A FAST INTEGRATED MOBILITY SPECTROMETER FOR RAPID MEASUREMENT OF SUB-MICROMETER AEROSOL SIZE DISTRIBUTION, PART I: DESIGN AND MODEL EVALUATION

Wang, J., Pikridas, M., Spielman, S. R., and Pinterich, T.

February 2017

Environmental & Climate Science Dept.

Brookhaven National Laboratory

U.S. Department of Energy
DOE Office of Science

DISCLAIMER

1 **A fast integrated mobility spectrometer for rapid measurement of sub-micrometer aerosol**

2 **size distribution, Part I: design and model evaluation**

3 Jian Wang[1][*], Michael Pikridas[1][†], Steven R. Spielman[2], Tamara Pinterich[1]

4 [1]Environmental and Climate Sciences Department, Brookhaven National Laboratory, Upton,

5 New York 11973, USA

6 [2]Aerosol Dynamics Inc., Berkeley, California 94710, USA

7 **Abstract**

8 A fast integrated mobility spectrometer (FIMS) was previously developed to characterize

9 submicron aerosol size distributions at a frequency of 1Hz and with high size resolution and

10 counting statistics (Kulkarni & Wang, 2006a, 2006b; Olfert, Kulkarni, & Wang, 2008).

11 However, the dynamic size range of the FIMS was limited to one decade in particle electrical

12 mobility. It was proposed that the FIMS dynamic size range can be greatly increased by using a

13 spatially varying electric field (J. Wang, 2009). This electric field creates regions with drastically

14 different field strengths in the separator, such that particles of a wide diameter range can be

15 simultaneously classified and subsequently measured. A FIMS incorporating this spatially

16 varying electric field is developed. This paper describes the theoretical frame work and

17 numerical simulations of the FIMS with extended dynamic size range, including the spatially

18 varying electric field, particle trajectories, activation of separated particles in the condenser, and

19 the transfer function, transmission efficiency, and mobility resolution. The influences of the

20 particle Brownian motion on FIMS transfer function and mobility resolution are examined. The

21 simulation results indicate that the FIMS incorporating the spatially varying electric field is

22 capable of measuring aerosol size distribution from 8 to 600 nm with high time resolution. The

23 experimental characterization of the FIMS is presented in an accompanying paper.

24 *Keywords:* Fast Integrated Mobility Spectrometer; Aerosol size distribution; High time

25 resolution; dynamic size range; Electrical mobility; Mobility resolution.

26

[*] Author to whom correspondence should be addressed: jian@bnl.gov
[†] Current affiliation: The Cyprus Institute, Environment Energy and Water Research Center, Nicosia, Cyprus

1 Introduction

Atmospheric aerosols play critical roles in air quality, public health, and visibility. In addition, they strongly influence climate by scattering solar radiation and by changing the reflectivity and lifetime of clouds. Real-time measurement of sub-micrometer aerosol size distribution is important in studies of aerosol properties and processes. Fast measurement is often necessary to capture transient aerosol dynamics, including those during nucleation and new particle formation processes. In addition, for measurements onboard mobile platforms such as research aircraft, high time resolution is often required to capture the spatial and temporal variations of atmospheric aerosols.

Existing techniques and instruments for measuring sub-micrometer aerosol size distributions are summarized in Kulkarni and Wang (2006a) and are briefly described here. Sub-micrometer aerosol size distributions are traditionally measured using Scanning Mobility Particle Sizers (SMPS) (S. C. Wang & Flagan, 1990). There have been many recent advancements in SMPS, including increased size resolution in nanometer size range (Chen et al., 1998; Flagan, 2004; Jiang et al., 2011; Rosser & de la Mora, 2005; Song & Dhaniyala, 2007), improved time resolution (Han, Chen, Pui, & Anderson, 2000; J. Wang, McNeill, Collins, & Flagan, 2002), and portability (Barmpounis, Maisser, Schmidt-Ott, & Biskos, 2016; Flagan, 2004; Steer, Gorbunov, Muir, Ghimire, & Rowles, 2014). Because SMPS measures one particle size at a time, the classifying voltage needs to be scanned over a wide range in order to cover the entire aerosol size distribution. This voltage scan typically takes a minimum of 60 s and is too slow for many applications (i.e., measurements onboard research aircraft). Electrical mobility-based instruments also include Electrical Aerosol Spectrometer (EAS, Tammet, Mirme, & Tamm, 2002), Engine Exhaust Particle Sizer (EEPS, Johnson, Caldow, Pocher, Mirme, & Kittelson, 2004; J. Wang et al., 2006), and Differential Mobility Spectrometer (DMS, Biskos, Reavell, & Collings, 2005), which measure particles of different mobilities simultaneously using a series of integrated electrometers. These instruments are capable of rapid measurement of aerosol size distribution, but their applications have largely been limited to aerosols with very high number concentrations (e.g., engine exhausts) due to the low sensitivity of electrometers. Besides low sensitivity, the size resolutions of EAS, EEPS, and DMS are considerably lower than that of SMPS. Recent developments in electrical mobility based instruments also include an Aspirating Drift Tube Ion

57 Mobility Spectrometer capable of measuring particle size distribution from 2 to ~ 12 nm within
58 several seconds (Oberreit, McMurry, & Hogan, 2014).

59   A Fast Integrated Mobility Spectrometer (FIMS) was developed previously for rapid
60 measurements of submicron aerosol size distribution under typical ambient concentrations
61 (Kulkarni & Wang, 2006a, 2006b). Inside the FIMS, charged particles of different electrical
62 mobilities are first separated by an electric field into different flow streamlines. The spatially
63 separated particles are subsequently grown into super-micrometer droplets inside a condenser.
64 The grown droplets are illuminated by a sheet of laser light and imaged by a CCD camera. In
65 addition to the number of particles, the images also provide particle position and therefore the
66 distance travelled by particle in the direction of the electric field, which directly relates to the
67 particle mobility. By counting particles of different electrical mobilities simultaneously, the
68 FIMS measures aerosol size distribution within 1 s, about two orders of magnitude faster than
69 traditional SMPS. Because individual particles are detected optically, the FIMS also provides
70 measurements with significantly higher signal to noise ratio compared to electrometer based
71 systems. The performance of the FIMS was characterized, and a data inversion technique was
72 developed to derive size distribution from FIMS data (Kulkarni & Wang, 2006b; Olfert et al.,
73 2008; Olfert & Wang, 2009). While capable of rapid measurement, the FIMS presented by
74 Kulkarni and Wang (2006a, 2006b) has a narrow dynamic size range limited to a factor of 3 to 5
75 in particle diameter (i.e., a factor of 10 in electrical mobility). As a result, measurements of sub-
76 micrometer size distribution (e.g., 15 to 1000 nm) require three FIMS units operated in parallel
77 with different separating voltages to cover the entire size range.

78   It was proposed that the dynamic size range of the FIMS can be increased without loss in
79 size and time resolutions by using a spatially varying electric field in the separator (J. Wang,
80 2009). This electric field creates regions with drastically different field strengths in the separator,
81 such that particles of a wide diameter range can be simultaneously classified and subsequently
82 measured. This is equivalent to combining into a single unit several original FIMS, operated with
83 different separating voltages. A FIMS incorporating this spatially varying electric field is
84 developed. Here we describe the theoretical framework and numerical simulations of the FIMS
85 characteristics, including the spatially varying electric field, particle trajectories, and activation
86 of particles inside the condenser. The dynamic size range, transmission efficiency, and transfer

87 function of the FIMS are derived from the simulations and discussed. The influences of the

88 particle Brownian motion on transfer function and mobility resolution are examined. The

89 experimental characterization of the FIMS is reported in an accompanying paper.

90

91 2 Instrument Design

92   The principle of the FIMS operating with a spatially varying electric field is essentially

93 the same as that of the original version described in Kulkarni and Wang (2006a), and is briefly

94 described below. The FIMS has three major sections - (i) separator, (ii) condenser, and (iii)

95 detector, where are arranged sequentially to form a continuous rectangular channel. A schematic

96 of the FIMS is present in Fig. 1 of J. Wang (2009). Particle-free sheath flow saturated with n-

97 heptanol enters the separator from a top entrance. Charged particles are carried into the separator

98 by a smaller aerosol flow through a narrow tangential slit. Inside the separator, the charged

99 particles are separated by the electric field into mobility-dependent trajectories. The spatially

100 separated particles subsequently enter the condenser. As no electric field is applied in the

101 condenser, particle positions in the channel cross section (i.e., x and y coordinates) essentially

102 remain unchanged downstream of the separator. The separated particles grow into super-

103 micrometer droplets in a supersaturated environment inside the condenser. At the exit of the

104 condenser, the grown droplets are illuminated by a laser sheet and imaged by a high-speed CCD

105 camera. The images provide the position of individual particles, which directly relates to the

106 particle mobility. As a result, particles of different mobilities/sizes can be measured

107 simultaneously. The original FIMS reported in Kulkarni and Wang (2006a and 2006b) employs a

108 uniform electric field, and its dynamic size range is limited to a factor of 10 in electrical mobility

109 in order to maintain a good size resolution (i.e., mobility resolution no less than 5).
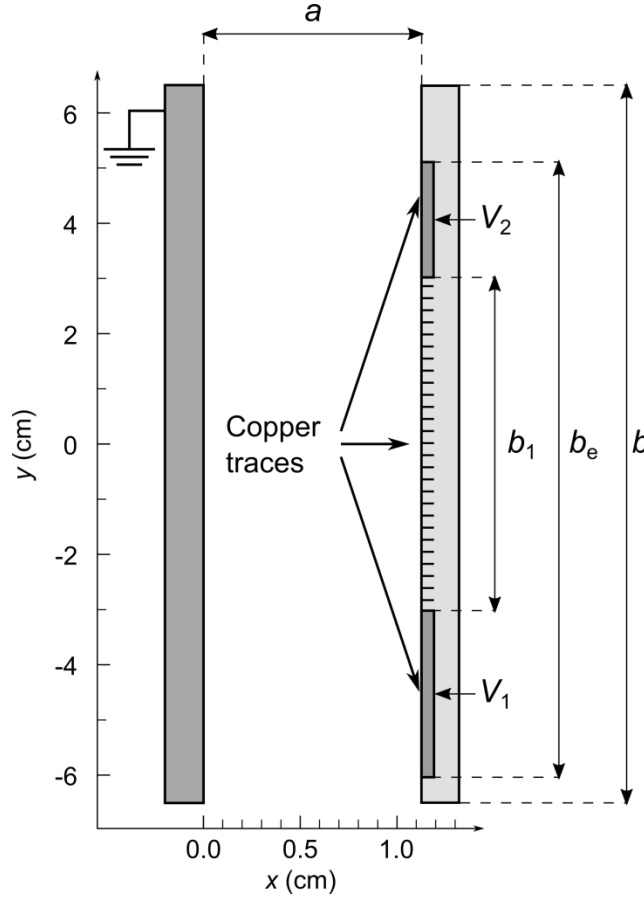
Figure 1. Schematic of the electrodes used to create the spatially varying electric field in the FIMS separator.

The development of the FIMS with improved dynamic size range involves two major modifications to the original FIMS. First, the original HV electrode, a solid aluminum plate, is replaced. J. Wang (2009) proposed an electrode where voltage applied varies exponentially as a function of y position (Note the coordinate system depicted in Fig. 1 of J. Wang (2009) is used in this study). However, such an electrode is very difficult to construct, if possible at all. Instead, a thick printed circuit board (PCB) with 61 straight copper traces running in the direction of the flow (z-direction) is used as the electrode. The diagram of this new electrode in the x-y plane (i.e., cross section of the separator channel) is shown in Fig. 1. The minimum voltage (V_1) of 20 V and maximum voltage (V_2) of 8000 V are applied to the first and last traces, which have a width of 3 cm and 2 cm, respectively. Fifty-nine thin traces of 0.15 mm in width are evenly spaced over a distance of 6 cm in the center (i.e., -3 cm $\leq y \leq$ 3 cm). Individual voltages ranging from 20 to 8000 V are generated by a network of resistor dividers, and applied to these 59 thin

5

125   traces. The voltage variation as a function of y position is shown in Fig. 2. The applied voltage

126   increases approximately exponentially with the y position of thin traces from 20 to 1800 V, then

127   increases linearly with y from 1800 to 8000 V. This is to reduce the voltage differences between

128   adjacent traces and to avoid arcing in the high voltage region. Only particles detected within the

129   viewing window (i.e., $0.2a \leq x \leq 0.8a$, -3.5 cm $\leq y \leq 3.5$ cm, where $a = 1.12$ cm, and represents

130   the gap between ground and HV electrodes) at the center of the channel cross section are used

131   for measurements, in order to avoid the edge effects of the electric and flow fields, and to

132   maintain good mobility resolution (Kulkarni & Wang, 2006a, 2006b). Note the voltage is

133   negative to separate positively charged particles, and the voltages presented here are absolute

134   values. The second major change is the increase of the length of the electrode (l_s), therefore the

135   separator. This is to increase the upper limit of particle size that could be measured by the FIMS.

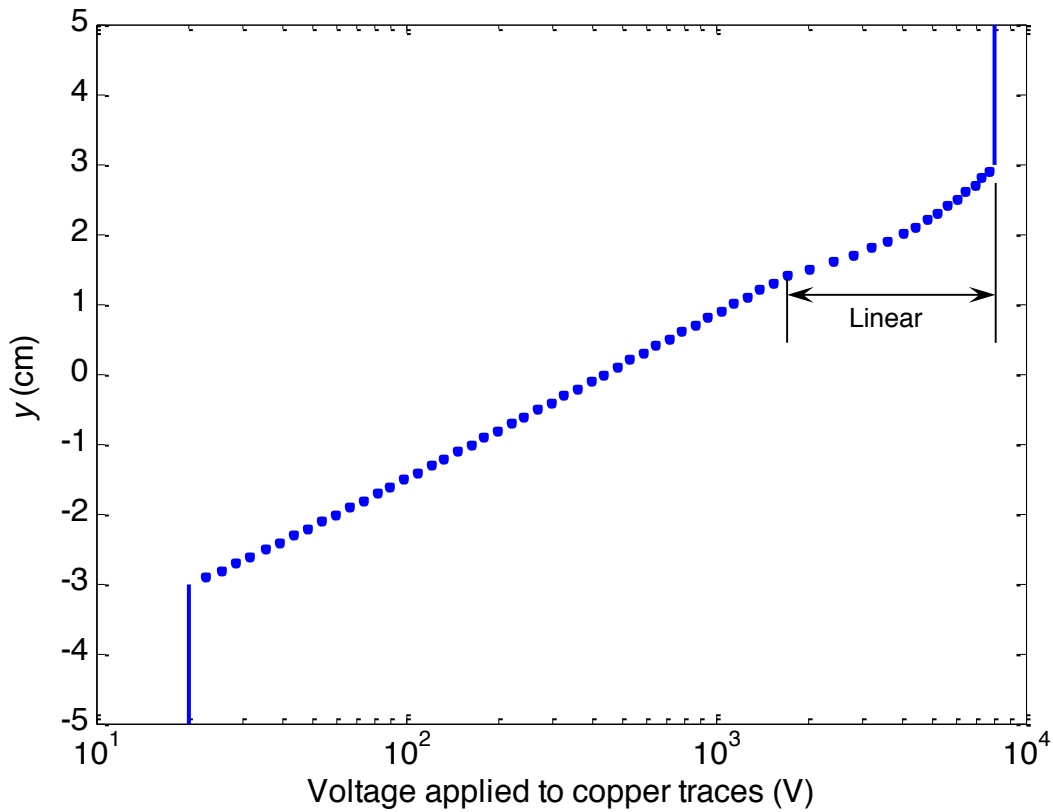136   Key physical dimensions and the operating parameters of the modified FIMS are given in Table

137   1.

138

139   Figure 2. Variation of the voltage applied to copper traces as a function of trace y position.

6

140

141 Table 1. Physical dimensions and parameters of the modified FIMS employing a spatially

142 varying electric field.

Description	Symbol	Values
Distance between separator electrodes	a	1.12 cm
Width of separator	b	12.70 cm
Length of the separating region	l_s	17.43 cm
Minimum Voltage	V_1	20 V
Maximum Voltage	V_2	8000 V
Width of the HV electrode (Fig. 1)	b_e	11.0 cm
Width of the area with 59 thin traces (Fig. 1)	b_1	6.0 cm
Sheath flow rate	Q_{sh}	13 L min^{-1}
Aerosol flow rate	Q_a	0.26 L min^{-1}
Viewing window x-coordinate range		0.2a to 0.8a
Viewing window y-coordinate range		-3.5 to 3.5 cm

143

3 Simulation of the characteristics of FIMS with enhanced dynamic size range

3.1 Spatially varying electric Field

146   The characteristics of the FIMS are examined using simulated particle trajectories inside
147 the instrument. The simulation of the particle trajectories requires the knowledge of the electric
148 field inside the separator. Unlike the idealized cases described in Wang (2009), the electric field
149 created by the new electrodes shown in Fig. 1 cannot be derived analytically, and was simulated
150 using COMSOL Multiphysics^{TM}. As the length of the electrodes (l_s) is much greater than the gap
151 between the two opposing electrodes (a), the electric field was assumed as constant along the z
152 direction (direction of the flow). The simulated 2-D electric field was then imported into
153 MATLAB^{TM} and interpolated to provide values at any given point in x-y space. Figures 3a and
154 3b show the simulated 2-D electric field and potential, respectively. The strength of the electric
155 field varies by a factor of ~500 (Fig. 3a). The electric field in the regions of $y < -3.0$ cm and $y >$
156 3.0 cm is largely uniform and has no appreciable y-component, due to constant voltages applied

157   to the both ends of the HV electrode. In contrast, the electric field in the center of the separator

158   cross section has a large *y*-component due to the strong spatial variation in applied voltage.

159   These features are consistent with those of idealized electric field presented in J. Wang (2009).

160
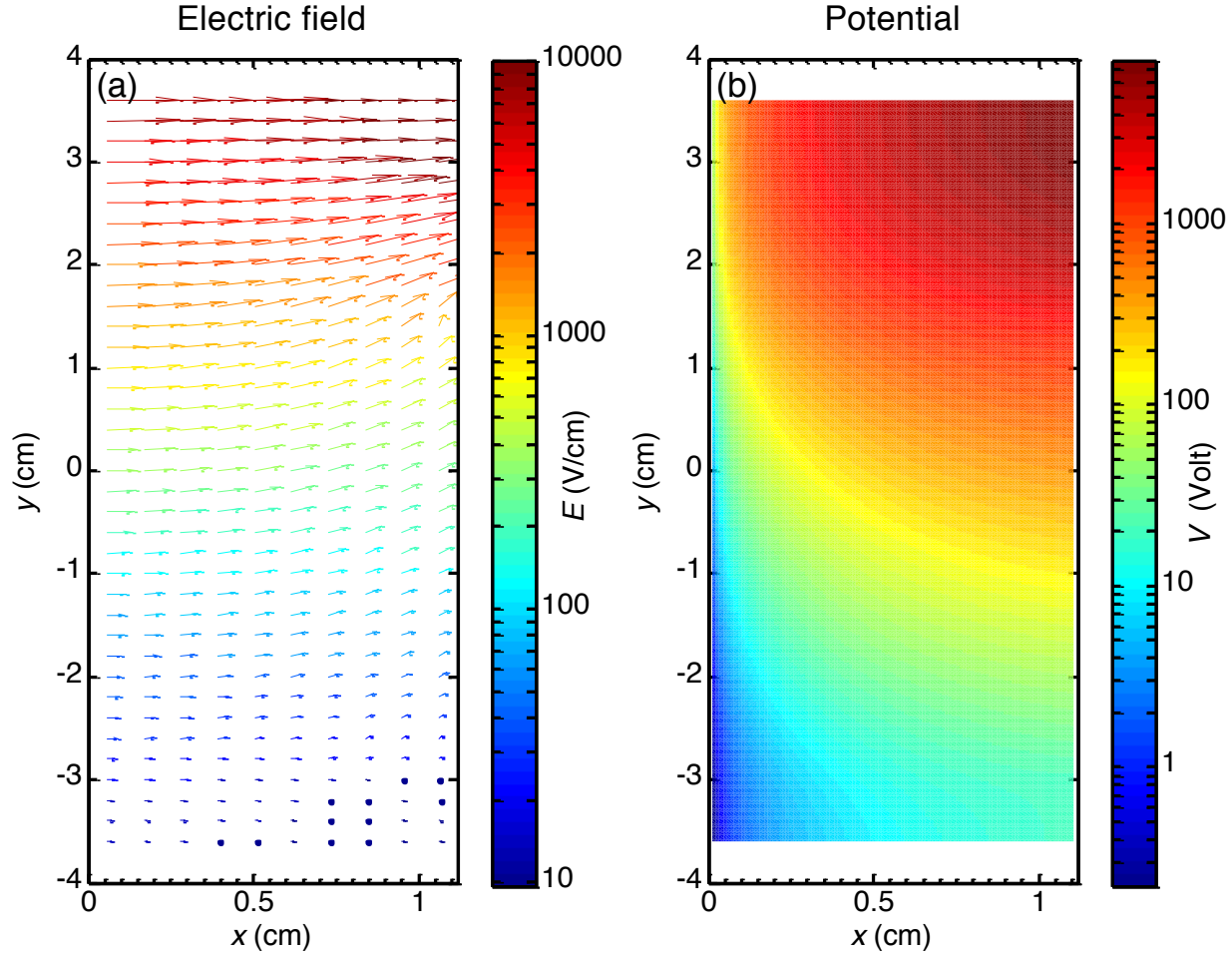
Figure 3. Simulated 2-D (a) electric field and (b) potential shown in *x-y* plane. Both the length
and the color of the field vector in plot (a) scale with the logarithm of the electric field strength.
The ground and HV electrodes are at *x*= 0 and 1.12 cm, respectively.

3.2 Simulation of particle trajectories inside FIMS

165   The particle trajectories inside the FIMS were simulated using the simulated 2D electric

166   field described above and assuming a well-developed 1-D flow field in the *z* direction:

167 $$u_z = \frac{6Q_t}{a^3 b} x(a-x) \tag{1}$$

168 where Q_t is effective total volumetric flow rate for the 1-D flow, and is given by:

169 $$Q_t = c\left(Q_{sh} + Q_a\right) \tag{2}$$

170 The factor c is included because the edge effects at the side walls of the separator (i.e., $y = \pm 0.5b$)
171 are neglected in the 1-D flow field. As the actual flow velocity near the side walls is lower, the
172 flow velocity in the center region, where particles are detected and counted (i.e., -3.5 cm < y <
173 3.5 cm), is higher than that assuming no edge effects. The adjustment factor c depends on the
174 dimension of the separator cross section, and has a value of 1.056 for this study (Olfert et al.,
175 2008). The motion of particles inside the FIMS was simulated using the Langevin equation
176 (Ermak, 1975),

177 $$\mathbf{r}(t+\Delta t) = \mathbf{r}(t) + [u_z\mathbf{k} + Z_p(D_p,\varphi,T,P)(E_x(\mathbf{r})\mathbf{i} + E_y(\mathbf{r})\mathbf{j})]\Delta t + \delta\mathbf{r}_G \tag{3}$$

178 Where $\mathbf{r}(t)$ and $\mathbf{r}(t+\Delta t)$ represent the particle's position at time t and $t + \Delta t$, respectively. E_x and
179 E_y are the x and y components, respectively, of the simulated 2-D electric field described above.
180 Z_p is the electrical mobility:

181 $$Z_p = \frac{qC_c}{3\pi\mu D_p} \tag{4}$$

182 where q is the electric charge on the particle, C_c is the Cunningham slip correction factor, μ is the
183 viscosity of the suspending medium (i.e., air), and D_p is the particle diameter. In this study, the
184 particle mobility is calculated at a temperature of 298.15K and a pressure of 1013.25 hPa. The
185 term $\delta\mathbf{r}_G$ in Eq. (3) corresponds to the particle Brownian displacement, and was simulated
186 individually for each particle by employing a Gaussian-shaped random number generator of zero
187 mean and standard deviation equal to $2D\Delta t$. D is the particle diffusion coefficient, and is related
188 to particle mobility by $D = Z_p k_B T / q$, where k_B is the Boltzmann constant, and T is the
189 temperature of the suspending medium.

190

191
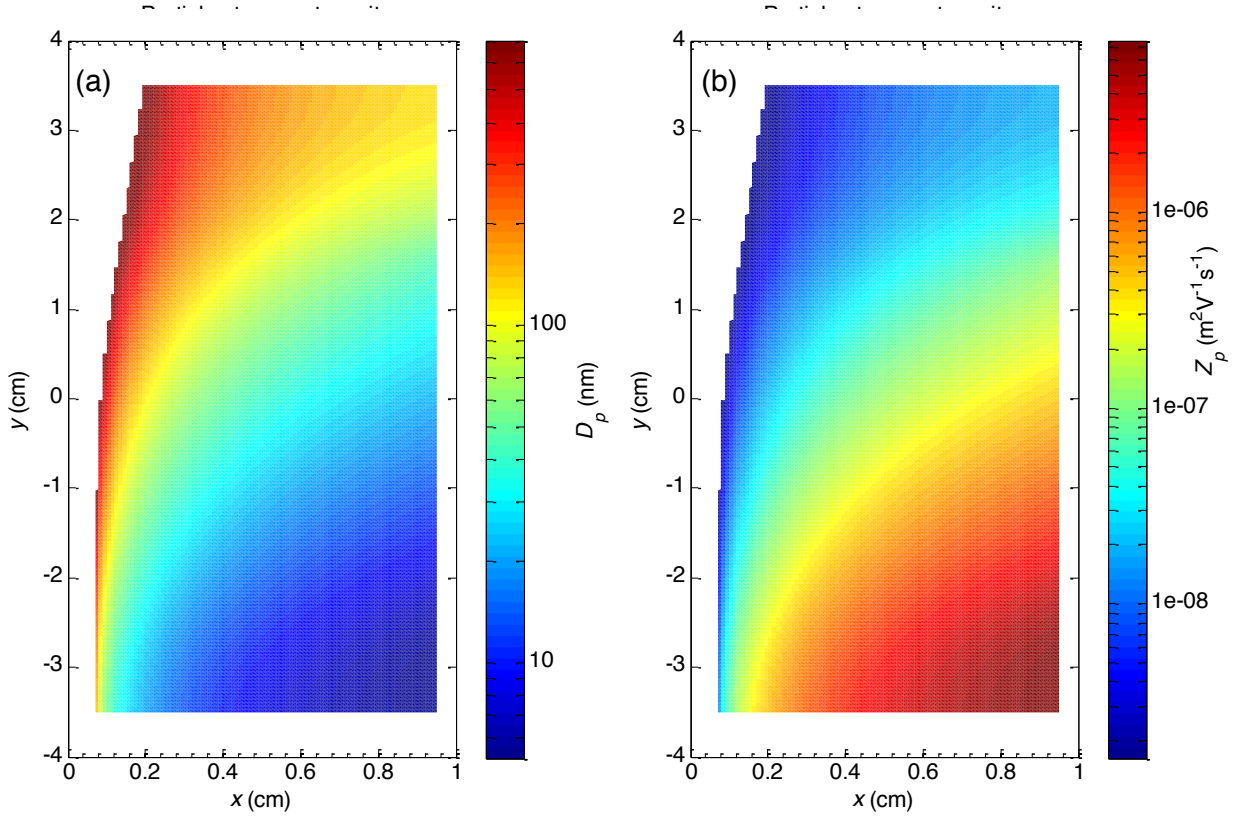
Figure 4. The *x-y* positions at the separator exit for non-diffusing particles introduced along the central aerosol inlet flow streamline, colored by (a) particle diameter and (b) electrical mobility.

194

3.3 Instrument response mobility of FIMS

As the FIMS measures a particle's mobility from its detected position (i.e., x and y coordinates) at the exit of condenser, an instrument response mobility is defined following the same approach as in Kulkarni and Wang (2006a) and J. Wang (2009) to facilitate the analysis of FIMS characteristics. Let $\Psi_{1,in}$ and $\Psi_{2,in}$ represent the two streamlines that bound the aerosol flow at the inlet (Kulkarni & Wang, 2006a), for a non-diffusing particle enters the separator along the central inlet flow streamline, $\Psi_{c,in} = \dfrac{\Psi_{1,in} + \Psi_{2,in}}{2}$, the instrument response mobility, Z_p^* , at the x-y position where the particle is detected is the same as the particle mobility Z_p.

10

203   Instrument response mobility (Z_p^*) was derived by simulating the trajectories of singly

204   charged, non-diffusion particles introduced at 1000 initial y positions (y_{in}) evenly spaced from -

205   4.0 and 4.0 cm along the central aerosol flow stream line. Particles introduced outside this y

206   range exit the condenser outside the viewing window (Table 1). The initial x position

207   corresponding to the central inlet flow streamline, x_{in} was derived from the following equation:

208    $$b \cdot \int_0^{x_{in}} u_z(x)dx = \int_0^{x_{in}} \frac{6Q_t}{a^3} x(a-x)dx = \frac{1}{2}Q_a \ .$$ (5)

209   At each y_{in} position, particles of 2500 different diameters logarithmically distributed from 4 to

210   900 nm were introduced, and their positions at the exit of the separator were determined by

211   simulating particle trajectories assuming no Brownian diffusion. For non-diffusing particles,

212   their x-y positions at the separator exit are the same as those detected following condensational

213   growth inside the condenser, where there is no electric field.

214   Figure 4 shows the x-y positions of these particles at the separator exit, colored by

215   particle diameter (Fig. 4a) and electrical mobility (Fig. 4b). By definition, Figure 4b shows the

216   map of instrument response mobility in the FIMS channel cross section. As expected, particles of

217   low electrical mobility (large particles) are classified in the upper region of the cross section

218   where the electric field is stronger, while in the lower region they remain close to the ground

219   electrode, where they were initially introduced. Particles of high electrical mobility (small

220   particles) in the upper region travel too fast and, they either are lost on the HV electrode or exit

221   the separator outside the viewing window. Small particles are instead classified in the lower

222   region where the field is weaker (Fig. 4).

223

224   **3.4 FIMS transfer function**

225   The FIMS transfer function $P\left(Z_p, Z_p^*\right)$ follows the same definition as in Kulkarni and

226   Wang (2006a) and J. Wang (2009), and is described as follows. The probability of a particle with

227   mobility Z_p introduced into the separator and being measured by the FIMS with instrument

228   response mobility from Z_p^* to $Z_p^* + dZ_p^*$ is $P\left(Z_p, Z_p^*\right)dZ_p^*$. As shown later, $P\left(Z_p, Z_p^*\right)$ often

229   peaks at $Z_p^*=Z_p$. To facilitate the comparison of transfer functions for different Z_p, we adopt a

230   slightly different form of transfer function, $P(Z_p, Z_p^*/Z_p)$. The two forms of the transfer

231   function are related to each other by $P(Z_p, Z_p^*/Z_p) = Z_p \cdot P(Z_p, Z_p^*)$. When particle Brownian

232   diffusion is taken into consideration, the transfer function also depends on the number of electric

233   charges carried by particles. For example, a doubly charged particle with the same electrical

234   mobility is larger therefore has a lower diffusivity than that of a singly charged particle. Here the

235   transfer function is derived based on singly charged particles. The derivation of the transfer

236   function for multiple-charged particles is very similar.

237   For the derivation of the FIMS transfer function, particle trajectories were simulated for

238   particles introduced at 1000 initial y positions evenly spaced from -4.0 to 4.0 cm, and at 100

239   initial x positions evenly distributed in the inlet flow streamline space between $\Psi_{1,in}$ and $\Psi_{2,in}$ that

240   bound the aerosol flow. The initial x positions ($x_{in,j}$, $0 \leq j \leq 99$) were derived using the following

241   equation (J. Wang, 2009):

242
$$b \cdot \int_0^{x_{in,j}} u_z(x)dx = \int_0^{x_{in,j}} \frac{6Q_t}{a^3} x(a-x)dx = \frac{(j+0.5)}{100} Q_a, \ 0 \leq j \leq 99. \tag{6}$$

243   Altogether, particles were introduced at a total of 100,000 initial positions. At each position, the

244   simulation of particle trajectories was repeated 10 times. Therefore a total of 1,000,000 particle

245   trajectories were simulated for each particle diameter. While no electric field is applied outside

246   the separator, particle position in the x-y plane may continue to vary due to Brownian motion,

247   especially for small particles. Therefore, the simulation of particle trajectory continued

248   downstream of the end of the electrode, to account for particle Brownian motion before

249   activation inside the condenser. Once activated, particles quickly grown to a sufficiently large

250   size (e.g., a few hundred nanometers) such that particle Brownian motion becomes negligible,

251   and the particle x-y position essentially remains unchanged afterwards. The distance traveled by

252   a particle between the end of electrode and the point of its activation (L_a) depends on particle

253   size and the supersaturation profile along the particle trajectory, therefore the particle position

254   within the channel cross section (i.e., x- y plane). The detected particle position was simulated

255   using fixed L_a of 5.9 and 13.5 cm, representing the minimum and maximum values, respectively.

256   The value of 5.9 cm includes a total length of 4.6 cm from end of the electrode to the end of the

257   separator and a 1.3 cm thick thermal insulation flange between the separator and condenser, and

258   represents the distance between the end of the HV electrode and the beginning of the condenser.

259   The value of 13.5 cm includes an additional distance of 7.6 cm into the condenser, which

260   presents the longest distance that a particle travels in the condenser before activation (8 nm

261   particles with trajectories near $x=0.5a$, Fig. 8b). The simulations using the two L_a values provide

262   the lower and upper limits of the impact of particle Brownian diffusion on the FIMS transfer

263   function. After the detected particle x-y positions were simulated, they were converted to

264   instrument response mobility Z_p^* using the map shown in Fig. 4b through interpolation. The

265   transfer function $P\left(Z_p, Z_p^*/Z_p\right)$ is simply the histogram of Z_p^*/Z_p for particles detected within the

266   viewing window, normalized by the number of the simulated particle trajectories and the width

267   of Z_p^*/Z_p bin, and scaled by a factor of 8/12.7. This factor is necessary because aerosol flow is

268   introduced into the separator over a length of 12.7 cm (in y direction) while in our simulations,

269   particles are introduced only within 8 cm width at the center of the channel.

270
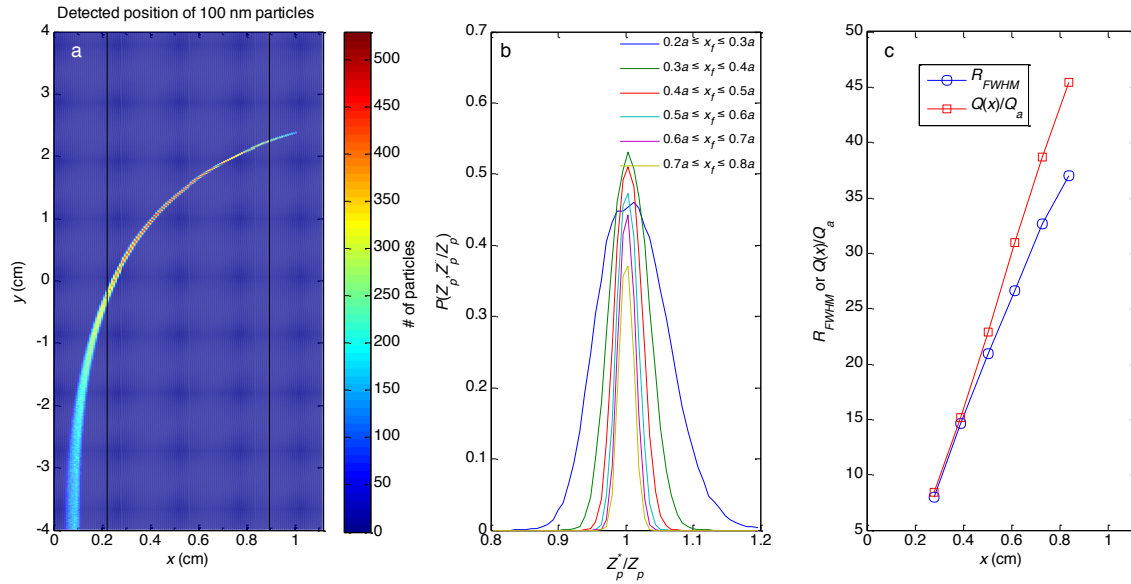
271   Figure 5 (a) Detected position of particles with diameter of 100 nm simulated with L_a=5.9 cm.

272   The color represents the number of particles within a 0.08 mm × 0.08 mm pixel. (b) Transfer

273   function of 100 nm particles detected within subareas of the viewing window. (c) Resolution

274   R_{FWHM} and the ratio of flow between the ground electrode and particle detection position (i.e.,

275      $Q(x)$) to aerosol flow rate.

13

276   The detected positions of particles with diameter of 100 nm simulated using L_a of 5.9 cm

277   are present in Fig. 5. Depending on its initial y position introduced at the aerosol inlet, particles

278   of same mobility experience electric forces of different strengths, leading to a range of final x

279   (and y) positions detected. Here we use x_f and y_f to denote the final detected particle x and y

280   positions, respectively. Using the same approach described above, the transfer functions for

281   particles detected within subareas of the viewing window were derived to gain insights into the

282   mobility resolution of the FIMS. Figure 5b and 5c show the transfer function and corresponding

283   mobility resolution R_{FWHM}, defined as the ratio of the particle mobility (Z_p) to the full width at

284   half maximum of the transfer function (Eqn. 28 of Kulkarni & Wang, 2006a), for 100 nm

285   particles detected in different subareas. The transfer function is narrower and the resolution is

286   higher for particles that migrate further in the x direction under a stronger electrical field. The

287   value of R_{FWHM} is consistent with the ratio of the rate of flow between the ground electrode (i.e.,

288   x=0) and particle x position to the aerosol flow rate, except in area with large x values where

289   resolution becomes limited by particle Brownian diffusion. This is consistent with R_{FWHM} of

290   FIMS employing an uniform electric field (Kulkarni & Wang, 2006a) and the finding of J. Wang

291   (2009), and suggests that measurements of high resolution may be achieved by using only

292   particles detected in subareas with high x values. The transfer function corresponding to the

293   entire viewing window is simply the sum of the transfer functions for particles detected in the 6

294   subareas shown in Fig. 5b, and has an overall R_{FWHM} value of 22.3.

295   Figure 6 shows the transfer function for particles with 5 diameters ranging from 10 to 200

296   nm. Transfer functions were simulated assuming no particle diffusion, and particle diffusion with

297   L_a of 5.9 and 13.5 cm, respectively. For non-diffusing particles, the transfer functions for 20, 50,

298   100, 200 nm particles are essentially the same, as the resolution for non-diffusing particles are

299   largely determined by particle final x position as discussed above (Kulkarni & Wang, 2006a; J.

300   Wang, 2009) . For these four sizes, particle final x positions range from $0.2a$ and $0.8a$ within the

301   viewing window. In comparison, the final x position of particles with a diameter of 10 nm is

302   greater than $0.35a$ even in the region with the weakest electric field, leading to an overall

303   narrower transfer function and a higher resolution. Particle Brownian diffusion has minor impact

304   on the transfer function for particles with diameters of 100 nm or larger, but leads to substantial

305   broadening of transfer function and therefore reduction in resolution when particle diameter is

306 less than 50 nm. It is worth noting that the difference in transfer functions simulated with the two

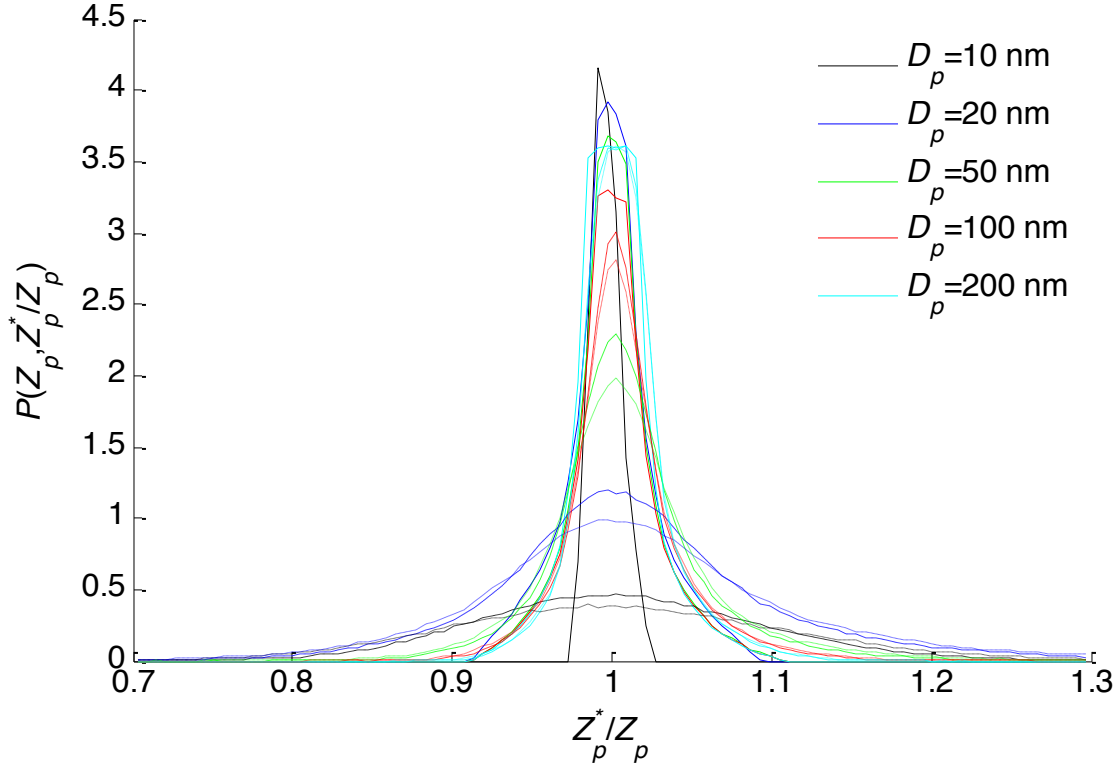307 different L_a values is quite minor.

308

309
310 Figure 6. Simulated FIMS transfer functions for particles with diameters of 10, 20, 50, 100, and
311 200 nm. The line colors correspond to different particle diameter. The solid, dashed, and dot
312 lines represent simulations assuming no particle diffusion, and particle diffusion with L_a of 5.9
313 and 13.5 cm, respectively.

314   Figure 7 shows the transmission efficiency (η_{trans}), and resolutions based on full width at
315 half maximum (R_{FWHM}) and standard deviation (R_{std}) as functions of particle diameter. The
316 resolution R_{std} is defined as the ratio of the particle mobility to the standard deviation of Z_p^*
317 calculated from the transfer function (i.e., Eqn. 20 in J. Wang, 2009). The transmission
318 efficiency represents the fraction of particles introduced into FIMS that have the final x-y
319 position within the viewing window, and is the integration of the transfer function over
320 instrument response mobility:

321 $$\eta_{trans} = \int P\left(Z_p, Z_p^*/Z_p\right) d\left(Z_p^*/Z_p\right)$$ (7)

322
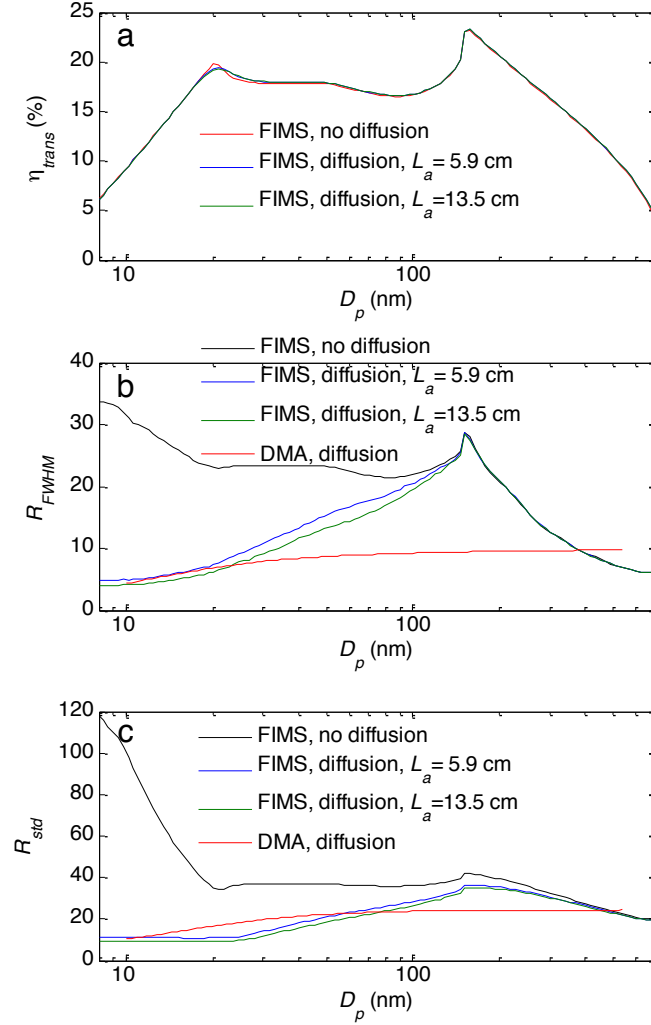
323 Figure 7. Simulated FIMS transmission efficiency (η_{trans}, panel a), resolution based on full width
324 at half maximum (R_{FWHM}, panel b), and resolution based on the standard deviation (R_{std}, panel c)
325 assuming no particle diffusion, and particle diffusion with L_a of 5.9 and 13.5 cm, respectively.
326 Also shown in panel b and c are corresponding resolutions of a DMA (Model 3081, TSI Inc.)
327 operated with Q_a and Q_{sh} of 0.5 and 5 L min^{-1}, respectively.

328 The results are shown for simulations assuming no particle diffusion, and particle diffusion with
329 L_a of 5.9 and 13.5 cm, respectively. As expected, particle Brownian diffusion has negligible

16

330   impact on η_{trans}. The transmission efficiency peaks at ~20 and ~ 150 nm, and shows a relatively

331   constant value of ~17% between. It decreases gradually below 20 nm and above 150 nm, and

332   reached ~7% at 8 and 600 nm. For non-diffusing particles, both R_{FWHM} and R_{std} decrease as

333   particle diameter D_p increases from 8 to 20 nm, remain relatively constant before reaching a local

334   maxima at ~150 nm, then decrease again from ~150 to 700 nm. These variations of $\eta_{trans,}$ R_{FWHM},

335   and R_{std} with D_p are essentially the same as those reported in J. Wang (2009). The explanations

336   for these variations are also detailed in J. Wang (2009). For example, the peak of η_{trans} at ~150

337   nm is due to the following reasons. At a given D_p, whether a particle can be detected within the

338   viewing window or not largely depends on the strength of the electric field experienced by the

339   particle in the separator. Because the strength of the electric field varies strongly with respect to

340   y coordinate, at a given D_p, only particles introduced within a certain range of initial y position

341   (y_{in}) are detected within the viewing window and contribute to η_{trans}. To a first order, η_{trans} is

342   proportional to this y_{in} range, which is referred to as the "effective" y_{in} range for the given D_p. At

343   D_p of 150 nm, the effective y_{in} range is $0.53 \leq y_{in} \leq 3.50$ cm (Δy_{in} = 2.97 cm), which includes the

344   entire region of the uniform strong electric field within the viewing window ($3.00 \leq y_{in} \leq 3.50$

345   cm, Fig. 2) as well as a region with spatially varying electric field ($0.53 \leq y_{in} \leq 3.00$ cm). We

346   note that 150 nm represents the lower diameter limit for particles that could be detected within

347   the viewing window in the region of the uniform strong electric field. As D_p decreases from 150

348   nm, an increasing fraction of particles introduced in the region of $3.00 \leq y_{in} \leq 3.50$ cm is detected

349   outside of the viewing window or collected by the HV electrode, leading to reduced η_{trans} (J.

350   Wang, 2009). As D_p increases above 150 nm and approaches the upper limit of the size

351   measurement range, the effective y_{in} range and η_{trans} also decrease because for particles near the

352   upper limit of measurement range, only those introduced in the region with the strongest electric

353   field are detected within the viewing window. For example, at a diameter of 400 nm, the

354   effective y_{in} range is reduced to $1.83 \leq y_{in} \leq 3.50$ cm. The above variations in the effective y_{in}

355   range lead to a peak in η_{trans} at ~150 nm. Another contributing factor is that the electrode voltage

356   varies linearly with y in the region of $1.40 \leq y_{in} \leq 3.00$ cm (Fig. 2) instead of exponentially as in

357   the region of $-3.00 \leq y_{in} \leq 1.40$ cm. The relatively slow variation of voltage and electric field

358   strength with y also increases the effective y_{in} range and therefore η_{trans} near 150 nm.

359

17

360   Particles with diameter of 150 nm that are introduced in the region of uniform strong

361   electric field have high x_f values (i.e., detected near the upper x limit of the viewing window,

362   $0.8a$), corresponding to high mobility resolutions (Fig. 5). Due to the contribution of these

363   particles with high x_f, the overall R_{FWHM} and R_{std} at 150 nm are higher than those of smaller

364   particles with effective y_{in} range entirely within the center region where the electric field varies

365   spatially. As D_p further increases from 150 nm, the x_f for particles introduced within the uniform

366   strong electric field region decreases, resulting in decreases of the overall R_{FWHM} and R_{std} (J.

367   Wang, 2009).

368

369   The impact of particle Brownian diffusion on mobility resolutions is quite minor for

370   particles with diameters greater than ~ 100 nm, but becomes increasingly significant as particle

371   diameter decreases. For particles smaller than 20 nm in diameter, particle Brownian diffusion

372   reduces R_{FWHM} from above 28 to below 7. There are minor differences between the resolutions

373   based on simulations using the two different L_a values, indicating the uncertainty in L_a has a

374   minor impact on simulated FIMS transfer function. The simulated FIMS resolutions are

375   compared with those of a SMPS operated with a diameter range of 10 - 540 nm (i.e., a TSI model

376   3081 DMA operated with a sheath and aerosol flow rates of 5 and 0.5 L min^{-1}, respectively, and

377   classifying voltage scanned from 10 to 10,000 V). Overall, the FIMS resolutions are generally

378   comparable to those of the SMPS. The FIMS R_{FWHM} is about the same as or better than that of

379   the SMSP for particles with diameter less than 400 nm. The FIMS R_{std} is higher/lower than that

380   of the SMPS for particles with diameters greater/less than 70 nm. The generally higher

381   resolutions of the FIMS, especially at large particle diameters, are mainly due to the higher

382   Q_{sh}/Q_a ratio of 50, compared to the ratio of 10 for typical SMPS.

383

384   **3.5 Activation of the particles inside the condenser**

385   The growth of the spatially separated particles in the condenser was simulated in a two-

386   step process. First, the temperature and heptanol vapor pressure fields inside the condenser were

387   simulated using the finite element modeling software package COMSOL Multiphysics®. As

388   only particles detected in the center region of the channel cross section (i.e., viewing window)

389   are used for measurements of particle size and concentration, the temperature T and vapor

18

390   concentration C were assumed to be independent of y coordinate, and were modeled as 2-

391   dimensional functions of x and z using the following convection-diffusion equations:

392
$$\mathbf{v} \cdot \nabla T = \alpha \nabla^2 T$$
$$\mathbf{v} \cdot \nabla C = D_v \nabla^2 C ' \qquad (8)$$

393   where α is the thermal diffusivity of air, and D_v is the molecular diffusivity of heptanol in air,

394   approximated as $D_v = -0.06478 + (T/3421.6 \text{ K}) + (T/1664.8 \text{ K})^2 \text{ cm}^2 \text{ s}^{-1}$ (Yaws, 2009). The

395   velocity field $\mathbf{v}$ was assumed to be fully developed as above, and has non-zero component only

396   in the z direction described by Eq. (1). For the boundary conditions, the temperature at the

397   entrance of the condenser was set at 24 °C, and C was set as 95% of the saturation concentration

398   of heptanol (Kemme & Kreps, 1969):

399      $C_{sat}(T) = \dfrac{1}{RT} 953.6 \text{ MPa} \cdot \exp\left(\dfrac{-2893.8 \text{ K}}{T - 133.5 \text{ K}}\right)$ (9)

400   The temperature of condenser walls was set at 4 °C (i.e., 20 °C below the incoming flow

401   temperature), and the heptanol concentration at the walls was set at the saturation concentration

402   at the wall temperature, which assumes that the wall surface is coated by condensed heptanol.

403

404   The simulated temperature and concentration fields were then imported into MATLAB$^{\text{TM}}$

405   and interpolated to provide values at any given point in the x-z plane. The growth of the droplets

406   along their trajectories in the condenser was simulated by numerically solving two coupled

407   ordinary differential equations in MATLAB$^{\text{TM}}$. The evolution of droplet diameter D_p is governed

408   by (Seinfeld & Pandis, 2006):

409      $\dfrac{dD_p}{dt} = \dfrac{4 D_v' M}{\rho} \dfrac{(C - C_s)}{D_p}$ (10)

410   where M and ρ are the molecular weight and density of heptanol, D_v' is the modified diffusivity

411   of heptanol in air accounting for non-continuum effects, and is given by

412      $D_v' = D_v \cdot \left[1 + \dfrac{2 D_v}{\alpha_c D_p}\left(\dfrac{2\pi M}{RT}\right)^{1/2} \right]^{-1}$, where α_c is the mass accommodation coefficient, and was

413   assumed as 1 (Seinfeld & Pandis, 2006). C_s represents the equilibrium heptanol concentration at

414   the surface of the growth droplets, and is given by $C_s = C_{sat}(T_s)\exp\left(\dfrac{4\gamma M}{\rho R T_s D_p}\right)$, where γ is the

19

415 surface tension of heptanol, and T_s is the temperature at droplet surface, which is governed by

416 (Chang & Davis, 1974):

417 $$\frac{dT_s}{dt} = \frac{3}{c_p \rho D_p}\left(H_{vap}\rho\frac{dD_p}{dt} - 4k_v'\frac{T_s - T}{D_p} \right)$$ (11)

418 where c_p and H_{vap} are the heat capacity and heat of vaporization of heptanol, respectively. k_v'

419 represents modified thermal conductivity of air and is calculated as

420 $k_v' = k_v\left[1 + \frac{2k_v}{\alpha_T D_p \rho_a c_{p,a}}\left(\frac{2\pi M_a}{RT} \right)^{1/2} \right]^{-1}$, where M_a, ρ_a, $c_{p,a}$, and k_v are the molecular weight, density,

421 heat capacity, and (continuum limit) thermal conductivity of air, respectively. α_T is thermal

422 accommodation coefficient, and is assumed to be unity (Seinfeld & Pandis, 2006). In Eqs. (10)

423 and (11), C and T are the vapor concentration and temperature fields simulated using COMSOL

424 Multiphysics® in the first step. For the simulation of droplet growth, the Brownian motion of

425 particles inside the condenser before activation was neglected, and because there is no electric

426 field in the condenser, the positions of growing droplets as they move along flow streamlines are

427 given by $x = x_0$, $z = u_z(x_0)t$, where x_0 is the initial x position as particles enter the condenser.

428

429 The saturation ratio of heptanol and droplet growth along the droplet trajectory (i.e., as a

430 function of z) are shown in Fig. 8 for different x positions. The entrance of the condenser is

431 represented by $z=0$, and droplets are illuminated and imaged at $z = 30.7$cm. Note the saturation

432 ratio is independent of y within the viewing window, and has reflective symmetry across the

433 center plane of $x=0.5a$. Therefore, the results are shown for particle trajectories with x positions

434 ranging from $0.1a$ to $0.5a$. For trajectories near the wall (e.g., $x =0.1a$), the saturation ratio

435 reaches a lower plateau after a shorter distance compared to that along trajectories close to the

436 center plane of the channel (i.e., $x =0.5a$). Near the entrance of the condenser, the saturation ratio

437 close to the wall is higher than that in the center of the channel, due to more rapid temperature

438 decrease of the flow near the wall (Fig. 8a). It is worth noting that particles of smaller sizes near

439 the center plane remain unactivated over a substantially longer distance (Fig. 8b-d), leading to

440 increased Brownian displacement therefore broadening of the transfer function as described

441 earlier. For the latter approximately two third of the condenser, the saturation near the center

plane of the condenser (i.e., x=0.5a) is substantially higher, due to heptanol vapor depletion near the wall. As a result, for particles of the same diameter, those with trajectories near the center plane grow to larger sizes despite a delayed start. The droplet growth and final droplet diameter (i.e., at z=30.7 cm) only strongly depend on x position near the condenser walls. For particles with same initial diameter, the final droplet diameter exhibits minor variations within the viewing window (i.e., 0.2a ≤ x ≤0.5a given the symmetry). For example, the final droplet diameters range from 1.9 to 2.3 μm for particles with diameter of 50 nm (Fig. 9). Along the same particle trajectory (i.e. x position), the final droplet diameter is also relatively insensitive to the initial particle diameter ranging from 8 to 600 nm, as expected for condensational droplet growth. The final droplet diameter is greater than 1.8 μm within the viewing window for particles as small as 8 nm, suggesting these droplets can be reliably detected optically.
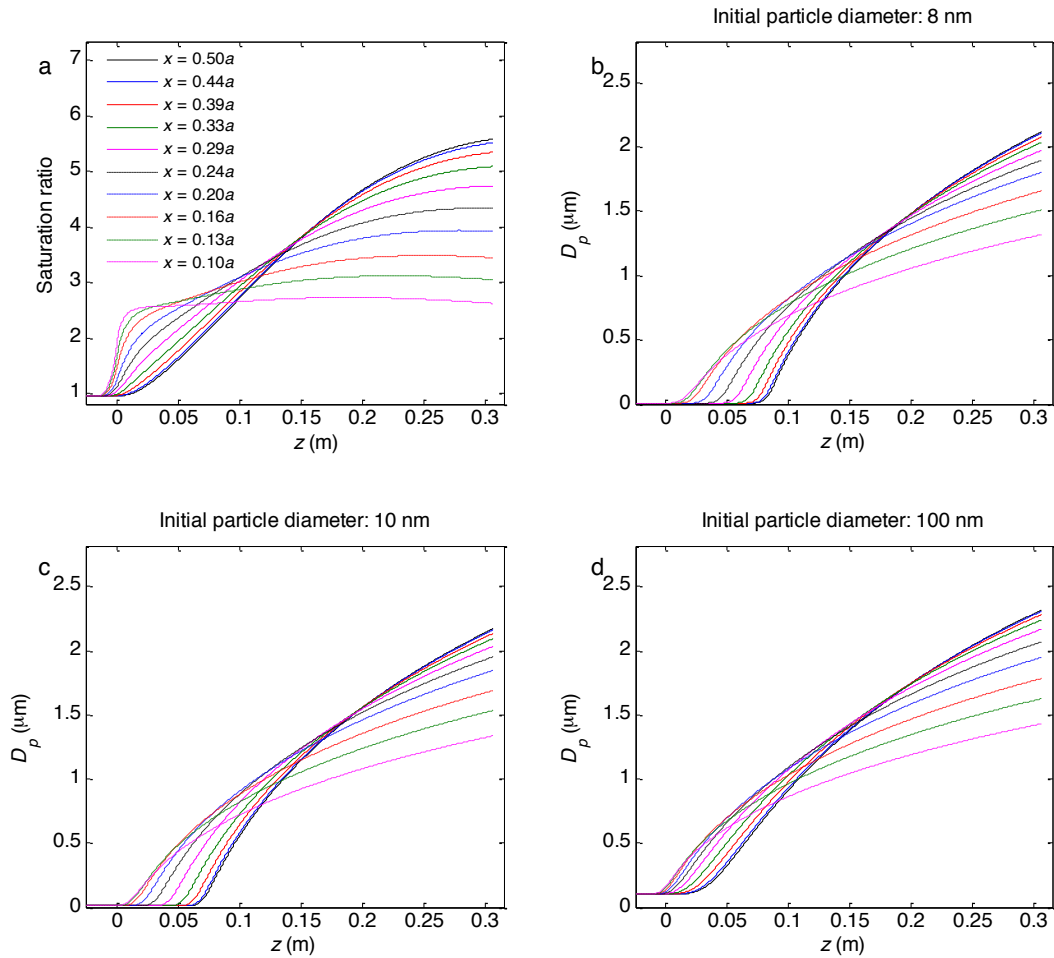

453

454 Figure 8. (a) Saturation ratio along particle trajectories inside the condenser for different *x*
455 positions, and diameters of growing droplets along trajectories starting with different *x* positions
456 for particles with initial diameters of (b) 8, (c) 10, (d) 100 nm, respectively. The entrance of the
457 condenser is represented by *z*=0, and droplets are illuminated and imaged at $z = 30.7$cm.
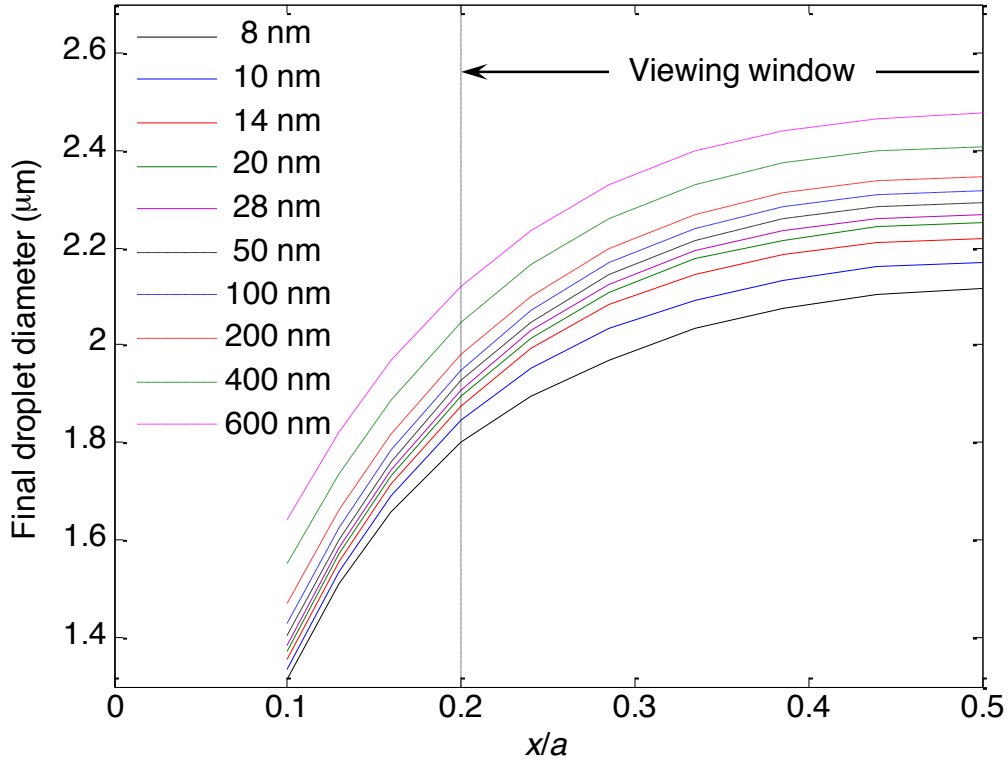
458

459

460 Figure 9. The final droplet diameter at the point of detection as a function of trajectory position
461 *x/a* for particles with diameters ranging from 8 to 600 nm.

462

463 **4 Summary**

464   A Fast Integrated Mobility Spectrometer employing a spatially varying electric field is
465 developed. In this first of a series of two papers, we present numerical simulations of the
466 characteristics and performances of the FIMS. The spatially varying electric field and particle
467 trajectories inside the FIMS were simulated, with Brownian motion of particles before activation

22

468   in the condenser taken into account. The simulation results indicate that the FIMS is capable of

469   measuring aerosol size distribution from 8 to 600 nm. Particle Brownian diffusion has minor

470   impact on the transfer function for particles with diameters of 100 nm or larger, while leads to

471   substantial broadening of transfer function and reduction in mobility resolution for particles with

472   diameters less than 50 nm. For the entire size range of 8 to 600 nm, simulated FIMS resolutions

473   are generally comparable to those of a typical TSI SMPS operated for a similar size range. The

474   growth of particles inside the condenser was simulated, the results show the final droplet

475   diameter are fairly insensitive to the particle position detected within the viewing window or the

476   initial particles diameters ranging from 8 to 600 nm. The final droplet diameter at the point of

477   detection is greater than 1.8 μm within the viewing window for particles as small as 8 nm,

478   suggesting the grown droplets can be reliably detected optically.

479

484

485

486

487

488   **References**

489   Barmpounis, K., Maisser, A., Schmidt-Ott, A., & Biskos, G. (2016). Lightweight differential
490   mobility analyzers: Toward new and inexpensive manufacturing methods. *Aerosol*
491   *Science and Technology, 50*(1). doi: 10.1080/02786826.2015.1130216

492   Biskos, G., Reavell, K., & Collings, N. (2005). Description and theoretical analysis of a
493   differential mobility spectrometer. [Article]. *Aerosol Science and Technology, 39*(6),
494   527-541. doi: 10.1080/027868291004832

495   Chang, R., & Davis, E. J. (1974). Interfacial conditions and evaporation rates of a liquid droplet.
496   *Journal of Colloid and Interface Science, 47*(1), 65-76. doi: 10.1016/0021-
497   9797(74)90080-0

498   Chen, D. R., Pui, D. Y. H., Hummes, D., Fissan, H., Quant, F. R., & Sem, G. J. (1998). Design
499   and evaluation of a nanometer aerosol differential mobility analyzer (Nano-DMA).
500   *Journal of Aerosol Science, 29*(5-6), 497-509. doi: 10.1016/s0021-8502(97)10018-0

501   Ermak, D. L. (1975). Computer simulation of charged particles in solution. I. Technique and
502   equilibrium properties. *J. Chem. Phys., 62*, 4189-4196.

503   Flagan, R. C. (2004). Opposed Migration Aerosol Classifier (OMAC). *Aerosol Science And*
504   *Technology, 38*(9), 890-899.

505   Han, H. S., Chen, D. R., Pui, D. Y. H., & Anderson, B. E. (2000). A nanometer aerosol size
506   analyzer (nASA) for rapid measurement of high-concentration size distributions.
507   [Article]. *Journal of Nanoparticle Research, 2*(1), 43-52. doi: 10.1023/a:1010014109495

508   Jiang, J. K., Attoui, M., Heim, M., Brunelli, N. A., McMurry, P. H., Kasper, G., . . . Mouret, G.
509   (2011). Transfer Functions and Penetrations of Five Differential Mobility Analyzers for
510   Sub-2 nm Particle Classification. *Aerosol Science and Technology, 45*(4), 480-492. doi:
511   10.1080/02786826.2010.546819

512   Johnson, T., Caldow, R., Pocher, A., Mirme, A., & Kittelson, D. B. (2004). A new electrical
513   mobility particle sizer spectrometer for engine exhaust particle measurements. *SAE*
514   *Technical Paper*, 2004-2001-1341. doi: 10.4271/2004-01-1341.

515   Kemme, H. R., & Kreps, S. I. (1969). Vapor pressure of primary n-Alkyl chlorides and alcohols.
516   *Journal of Chemical and Engineering Data, 14*(1), 98-&. doi: 10.1021/je60040a011

517   Kulkarni, P., & Wang, J. (2006a). New fast integrated mobility spectrometer for real-time
518   measurement of aerosol size distribution - I: Concept and theory. *J. Aerosol Sci., 37*(10),
519   1303-1325.

520   Kulkarni, P., & Wang, J. (2006b). New fast integrated mobility spectrometer for real-time
521   measurement of aerosol size distribution: II. Design, calibration, and performance
522   characterization. *Journal of Aerosol Science, 37*(10), 1326-1339.

523 Oberreit, D. R., McMurry, P. H., & Hogan, C. J. (2014). Mobility Analysis of 2 nm to 11 nm
524   Aerosol Particles with an Aspirating Drift Tube Ion Mobility Spectrometer. *Aerosol*
525   *Science and Technology, 48*(1), 108-118. doi: 10.1080/02786826.2013.861893

526 Olfert, J. S., Kulkarni, P., & Wang, J. (2008). Measuring aerosol size distributions with the fast
527   integrated mobility spectrometer. *Journal of Aerosol Science, 39*(11), 940-956.

528 Olfert, J. S., & Wang, J. (2009). Dynamic Characteristics of a Fast-Response Aerosol Size
529   Spectrometer. *Aerosol Science And Technology, 43*(2), 97-111.

530 Rosser, S., & de la Mora, J. F. (2005). Vienna-type DMA of high resolution and high flow rate.
531   *Aerosol Science and Technology, 39*(12), 1191-1200. doi: 10.1080/02786820500444820

532 Seinfeld, J. H., & Pandis, S. N. (2006). *Atmospheric Chemistry and Physics* (2nd ed.). Hoboken:
533   John Wiley & Sons, Inc.

534 Song, D. K., & Dhaniyala, S. (2007). Nanoparticle cross-flow differential mobility analyzer
535   (NCDMA): Theory and design. *Journal of Aerosol Science, 38*(9), 964-979. doi:
536   10.1016/j.jaerosci.2007.07.004

537 Steer, B., Gorbunov, B., Muir, R., Ghimire, A., & Rowles, J. (2014). Portable Planar DMA:
538   Development and Tests. *Aerosol Science and Technology, 48*(3), 251-260. doi:
539   10.1080/02786826.2013.868863

540 Tammet, H., Mirme, A., & Tamm, E. (2002). Electrical aerosol spectrometer of Tartu
541   University. *Atmospheric Research, 62*(3-4), 315-324. doi: 10.1016/s0169-
542   8095(02)00017-0

543 Wang, J. (2009). A fast integrated mobility spectrometer with wide dynamic size range:
544   Theoretical analysis and numerical simulation. *J. Aerosol Sci., 40*(10), 890-906.

545 Wang, J., McNeill, V. F., Collins, D. R., & Flagan, R. C. (2002). Fast mixing condensation
546   nucleus counter: Application to rapid scanning differential mobility analyzer
547   measurements. [Article]. *Aerosol Science and Technology, 36*(6), 678-689. doi:
548   10.1080/02786820290038366

549 Wang, J., Storey, J., Domingo, N., Huff, S., Thomas, J., & West, B. (2006). Studies of diesel
550   engine particle emissions during transient operations using an engine exhaust particle
551   sizer. [Article]. *Aerosol Science and Technology, 40*(11), 1002-1015. doi:
552   10.1080/02786820600919408

553 Wang, S. C., & Flagan, R. C. (1990). Scanning electrical mobility spectrometer. *Aerosol Sci.*
554   *Technol., 13*(2), 230-240.

555 Yaws, C. L. (2009). *Transport Properties of Chemicals and Hydrocarbons* (1st ed.): Elsevier
556   Inc.

557